Accuracy of high resolution coastal flow speed simulations during and outside of wind, wave and stratification events (Gulf of Lion, NW Mediterranean)

Elise Vissenaekens, Katell Guizien, Xavier Durrieu de Madron, Ivane Pairaud, Yann Lerredde, Pere Puig, François Bourrin

Accuracy of high resolution coastal flow speed simulations during and outside of wind, wave and stratification events (Gulf of Lion, NW Mediterranean)

Elise Vissenaekens[a], Katell Guizien[a,*], Xavier Durrieu de Madron[b], Ivane Pairaud[c], Yann Leredde[d], Pere Puig[e], François Bourrin[b]

[a] *CNRS-Sorbonne Université, Laboratoire d'Ecogéochimie des Environnements Benthiques, LECOB, Observatoire Océanologique, 1 avenue Pierre Fabre, Banyuls Sur Mer, 66650, France*

[b] *CNRS-Université Perpignan Via Domitia,, Centre de Recherche et de Formation sur les Environnements Méditerranéens, CEFREM, 52 avenue Paul Alduy, Perpignan, 66860, France*

[c] *Institut Français de Recherche pour l'Exploitation de la Mer, IFREMER, Laboratoire Environnement Ressources Provence Azur Corse, BP 330, La Seyne sur Mer, 83507, France*

[d] *CNRS–Université Montpellier-2, Géosciences Montpellier, place Eugène Bataillon, Montpellier Cedex 5, 34095, France*

[e] *ICM-CSIC, Passeig Marítim de la Barceloneta 37–49, Barcelona, 08003, Spain*

Abstract

Accurately predicting the flow speed is crucial for applications of coastal ocean circulation simulations such as sediment, larval or contaminant dispersal. This study aims to assess the accuracy of simulated flow speed in a coastal circulation model in comparison with field observations. Deviation between simulated and observed flow speed was assessed in four shallow, coastal locations and four deep, offshore locations in the Gulf of Lion (NW Mediterranean Sea) using six indicators (bias, relative bias, root mean square error, Hanna & Heinold index, correlation and scatter index). Statistical dis-

*Corresponding author: guizien@obs-banyuls.fr

tributions of indicators were calculated during reference periods with low wind, no waves and no stratification. During these periods, relative bias indicated the model displayed a higher performance in predicting transport at shallow stations than at deep stations probably due to grid refinement at these stations. However, there was a low correlation between simulated and observed flow speed, indicating short term time/space mismatches, at all stations during reference periods. Indicators were then calculated during three types of events (wind, waves and stratification) when model assumptions were expected to be violated and their corresponding probability during reference periods indicated that neither wind, wave nor stratification events worsens model's performance.
Keywords: Coastal circulation, modelling, flow speed, uncertainty quantification, Mediterranean, Gulf of Lion

1. Introduction

Ocean currents are the key drivers of dissolved and particulate compound transport. At the global scale, the thermohaline circulation regulates the earth's climate (McCarthy et al., 2015; Clark et al., 2019). Wind-driven, upwelling currents arrange nutrient transport and mixing and regulate primary production at the regional scale (Falkowski et al., 1998). From regional to coastal scales, ocean currents play an imperative role in sediment transport and pollution diffusion (James, 2002; Dufois et al., 2008; Warner et al., 2008; Mansui et al., 2020). At all spatial scales, vessel navigation and marine population connectivity (from large mammal migration to benthic species' larval dispersal) are affected by ocean currents (Cowen et al., 2000; Briton

et al., 2018; Putman, 2018; Mannarini and Carelli, 2019). These applications are currently simulated with Lagrangian dispersal models which, in contrast to Eulerian models, disregard mixing processes and only account for transport processes. Unfortunately, ocean velocity observations, which are necessary to describe these transport processes, are often limited in either time or space. Satellite-mounted altimeters and radars, land-based radars and Lagrangian drifters can measure the currents over a wide area, but only near the ocean's surface (Dohan et al., 2010; Mader et al., 2016). Some in situ current meters do provide flow measurement time series along vertical profiles (e.g. Acoustic Doppler Current Profiler, ADCP), but single point measurements are still common (Schroeder et al., 2013; Durrieu De Madron et al., 2019). ADCPs which were previously only deployed at fixed moorings (Guizien et al., 1999) are now being mounted on the hulls of ships (Système Acquisition Validation Exploitation de Données des Navires de l'INSU - Projet SAVED https://sextant.ifremer.fr/record/6f6e95e9-8e97-48d6-b536-b40f2ad87402/, accessed 04/06/2021) or on autonomous underwater vehicles (Dohan et al., 2010; Bourrin et al., 2015; Gentil et al., 2020). Ultimately, ocean current measuring devices are either deployed on the horizontal or on the vertical plane, which strongly limits their applicability to study transport processes. For this reason, transport processes are mainly studied using current simulations over the entire ocean. Ocean circulation models vary according to the different scales and processes they aim to simulate. Tide models are bidimensional models, predicting sea surface elevation and depth-integrated horizontal flow transport, whose main application is navigation (Le Provost and Lyard, 2000). Global ocean circulation mod-

els (OGCMs) are three-dimensional models resolving the ocean dynamics at coarse spatial scales everywhere on earth (1/12 °). They either rely on atmospheric coupling for climate predictions (Siedler et al., 2001; Chassignet et al., 2007; Somot et al., 2008) or on one-way atmospheric forcing for modelling ocean energy, fishery management and ship routing (Drévillon et al., 2018). Coastal circulation models are three-dimensional models forced by atmospheric models, most of the time without air-sea interaction, simulating the ocean flow dynamics and hydrology on a limited area. These models aim to simulate meso-scale to sub-meso-scale ocean processes, like eddies (Hu et al., 2009, 2011), dense water cascading (Ulses et al., 2008) and river plumes (Marsaleix et al., 1998). They use a spatial resolution that reaches about 100 m in the horizontal and 1 m in the vertical (Dumas and Langlois, 20O9; Briton et al., 2018). Such models are considered capable of describing the processes controlling the transport of dissolved and/or particulate matter in a variety of applications (oil spills, land-sea transfer, ecosystem modelling, population connectivity). Regional circulation models have also been coupled to wave models for sediment transport and beach erosion prediction (Ulses et al., 2008; Dufois et al., 2008; Warner et al., 2008). Examples of these models are the Model for Applications at Regional Scale (MARS 3D, Lazure and Dumas, 2008; Dumas and Langlois, 20O9), the COupled Hydrodynamical Ecological model for REgioNal Shelf seas (COHERENS, Drévillon et al., 2018), the Regional Ocean Modelling System (ROMS, Moore et al., 2011) and SYMPHONIE (Marsaleix et al., 2008, 2009a).

However, circulation simulations are subject to various sources of uncertainties, either linked to the model's implementation or to the model's

intrinsic assumptions. The model's implementation includes the spatial and temporal resolution of the baroclinic modes and the precision of the forcing data (atmospheric forcing, river runoff, bathymetry and open-boundary forcing). The sensitivity to the grid's spatial resolution (Kirtman et al., 2012; Kvile et al., 2018; Cai et al., 2020) and to atmospheric and open boundary forcing (Kourafalou et al., 2009) has been thoroughly illustrated. In addition to uncertainties coming from model implementations, uncertainties can come from the model's intrinsic assumptions, such as hydrostaticity, the Boussinesq approximation, the turbulent closure scheme and air-sea interaction. The hydrostatic assumption that the vertical variation of the pressure is dominated by gravity acceleration (resulting in negligible vertical velocities compared to horizontal ones) is not met during wave events (Marshall et al., 1997; Zhang et al., 2014). The Boussinesq approximation (density variations can be neglected except in the terms associated with buoyancy forcing) may not be met in the upper stratified ocean, since water density can vary up to 5%, particularly in coastal areas under riverine influence. Therefore, the Boussinesq approximation can cause inaccuracies in the Eulerian simulated velocity of the same magnitude as the water density variation (McDougall et al., 2002). Turbulence closure is also a vital part of any flow dynamics model as it distributes the total flow energy between the turbulent energy resulting from all velocity fluctuations at the subgrid scale and the mean flow (Boussinesq, 1903; Prandtl, 1925). This splitting of the flow energy is essential to describe transport and mixing processes in the numerical simulations. Turbulence closure is expected to play a more prominent role when energetic transfer happens at scales smaller than the spatio-temporal grid,

such as during wind-wave (Fisher et al., 2018) or river flooding events (Reffray et al., 2004). Evaluating model accuracy during selected events when the classical assumptions of ocean models aren't met has been frequent practice in the coastal modelling community over the last two decades (Marsaleix et al., 1998; Estournel et al., 2001; Reffray et al., 2004; Petrenko et al., 2005; Ulses et al., 2008; Estournel et al., 2016, in the Gulf of Lion). Nevertheless, to disentangle uncertainties due to model assumption violation from those related to implementation, it is necessary to quantify the uncertainty of the model when the assumptions are valid. To our knowledge, this has never been done together and actually, implementation uncertainties on predictied flow speed have been assessed qualitatively only (André et al., 2005; Petrenko et al., 2005; Schaeffer et al., 2011, in the Gulf of Lion).

In the present study, we assessed the uncertainties of regional circulation speed simulations performed in the NW Mediterranean Sea with the hydrostatic Boussinesq model SYMPHONIE (S26 version, https://sirocco.obs-mip.fr/ocean-models/s-model/download/), implemented at one of the finest spatio-temporal resolution to date for bathymetry, atmospheric data and river data. The simulations, which were performed from January 2010 to June 2013, were compared to hydrodynamic observations available in the area during this period. Uncertainties in flow speed in different locations and periods were assessed when the model's assumptions were valid (reference period in absence of wind, waves and stratification) and when assumptions were violated (strong wind events, wave events and stratification events). Model performance was systematically assessed by comparing six indicators calculated during each event type and observation station to their statistical

distribution outside of these events.

2. Material and methods

2.1. Study area

The Gulf of Lion is located in the northwestern part of the microtidal Mediterranean Sea and has a wide continental shelf with a mean depth of 70 m (Aloisi et al., 1973). It is delineated by a steep shelf break, incised by a dense network of submarine canyons (Figure 1). Its coastal circulation mainly results from the interaction between the thermohaline Northern Current, which flows along the shelf break from the northeast to the southwest and the frequent continental winds blowing from the north and northwest (Mistral and Tramontane resp.), which induce winter convection (Millot, 1990). The south-easterly and southerly winds, which blow less frequently, occur mainly from autumn to spring and can cause large swells (Guizien, 2009). The Gulf of Lion's coastal circulation is also influenced by the outflow of one of the largest Mediterranean rivers, the Rhône River, and a series of smaller rivers with typical Mediterranean flash-flooding regimes (Guizien et al., 2007; Ludwig et al., 2009). The size of the freshwater plume from the Rhône River depends on the atmospheric conditions, the strength of the river flow and the sea water circulation (Millot, 1990; Many et al., 2016, 2018). The surface layers in the Gulf of Lion can stratify thermally between spring and autumn and are recurrently destabilised nearshore by coastal upwelling (Millot, 1990; Petrenko et al., 2005).

2.2. Water current observations

Horizontal velocity measurements were gathered from eight locations in the Gulf of Lion between January 2010 and June 2013 (Figure 1). Observations included the shallow coastal ADCP moorings BeSete, Mesurho, POEM, and SOLA and the deep moorings Planier, Cap de Creus (Creus), Lacaze-Duthiers (LD) and Lion with one or more single point, acoustic Doppler current meters (SP-ADCMs). The time periods for which flow speed data was acquired are given in Table 1. Additional information on the observations, such as equipment specifications, can be found in the appendix Table A.1.

The observations were filtered to remove erroneous data. For the deep stations, if the velocity measurements presented abnormal values (defined as spikes of intensity with respect to the daily average greater than three times the standard deviation), they were replaced by the average of the previous and the following valid value. For the shallow stations, the upper three meters of the water column were not taken into account, to avoid measuring air speed amid sea surface fluctuations. Moreover, all observations were filtered over time to detect unrealistically fast changes in water speed. The maximum change in water speed tolerated was 30 cm/s over one hour. Another filter was applied on the vertical level and the maximum change in water speed tolerated was 10 cm/s over one meter.

2.3. Ocean circulation simulations

The free surface ocean model SYMPHONIE (Marsaleix et al., 2009a,b, 2012, SIROCCO, https://sirocco.obs-mip.fr/ocean-models/s-model/, accessed 17/05/2021) was set up to perform regional ocean circulation simulations at a very high resolution in the Gulf of Lion (Briton et al., 2018). The model solves

hydrostatic primitive equations with a finite-difference method on a C curvilinear grid under Boussinesq approximation and with an energy conserving numerical scheme (Marsaleix et al., 2008). Wave-coupling was not activated and turbulent closure scheme was set to two-equation K-ϵ (Michaud et al., 2012). A bipolar, curvilinear, 680x710 horizontal grid was used to mesh the Gulf of Lion yielding a resolution of 80 m at the coast and 2.7 km in the open ocean (Figure 1, Bentsen et al., 1999). Generalized σ-coordinates were used for vertical meshing, with 29 vertical levels (Briton et al., 2018). Simulations were carried out over the period January 2010- June 2013 and were forced by sea-surface dynamical downscaling of the ERA-Interim atmospheric reanalysis by the regional climate model ALADIN-Climate (ALDERA, 12 km horizontal and 3 h temporal resolutions) and by open-sea boundary conditions from the hindcast downscaled simulation NM12-FREE ($\sim$ 7 km horizontal resolution, Hamon et al., 2016). Observed daily discharge of nine rivers (Var, Grand Rhône, Petit Rhône, Hérault, Orb, Aude, Agly, Têt, Tech; http://www.hydro.eaufrance.fr/, accessed 17/05/2021) were included as well. The model's internal and external timesteps were 25.48s and 1.59s, respectively. The simulated velocities were extracted four times per hour on minute 0, 20, 30 and 40 to correspond with the times the observations were measured. On the horizontal, the simulated flow speeds were extracted at the grid point closest to the observations' location (less than 132 m apart). On the vertical, since the simulation's vertical levels did not match the observations' depths, the simulated speeds were interpolated at the same depth as the observations. If the actual water depth was larger than the water depth in the simulation (bathymetric discrepancy), the simulated speeds were in-

terpolated at the depth with the same distance from the bottom as the observation.

2.4. Statistical indicators

The deviation between observed O_{ij} and simulated M_{ij} current speed at depth i and time j was described by six time- and depth-averaged statistical indicators, calculated as follows:

$$Bias = \frac{\Sigma_{i=1}^{N_d}\Sigma_{j=1}^{N_t}(M_{ij} - O_{ij})}{N_d N_t} \tag{1}$$

$$RelativeBias = \frac{\Sigma_{i=1}^{N_d}\Sigma_{j=1}^{N_t}(M_{ij} - O_{ij})}{\sqrt{N_d N_t \Sigma_{i=1}^{N_d}\Sigma_{j=1}^{N_t} M_{ij} O_{ij}}} \tag{2}$$

$$RMSE = \sqrt{\frac{\Sigma_{i=1}^{N_d}\Sigma_{j=1}^{N_t}(M_{ij} - O_{ij})^2}{N_d N_t}} \tag{3}$$

$$HH = \sqrt{\frac{\Sigma_{i=1}^{N_d}\Sigma_{j=1}^{N_t}[(M_{ij} - O_{ij})^2}{\Sigma_{i=1}^{N_d}\Sigma_{j=1}^{N_t} M_{ij} O_{ij}}} \tag{4}$$

$$SI = \sqrt{\frac{\Sigma_{i=1}^{N_d}\Sigma_{j=1}^{N_t}[(M_{ij} - \bar{M}) - (O_{ij} - \bar{O})]^2}{\Sigma_{i=1}^{N_d}\Sigma_{j=1}^{N_t} M_{ij} O_{ij}}} \tag{5}$$

$$Correlation = \frac{\Sigma_{i=1}^{N_d}\Sigma_{j=1}^{N_t}[(M_{ij} - \bar{M}).(O_{ij} - \bar{O})]^2}{\sqrt{\Sigma_{i=1}^{N_d}\Sigma_{j=1}^{N_t}(M_{ij} - \bar{M})^2 . \Sigma_{i=1}^{N_d}\Sigma_{j=1}^{N_t}(O_{ij} - \bar{O})^2}} \tag{6}$$

with $\bar{O}$ the observed current speed averaged over depth and time and $\bar{M}$ the simulated current speed averaged over depth and time.

The bias (equation 1) is the difference between the simulated and observed mean. It indicates systematic under- (negative value) or overestimation (positive value) of the simulated flow speed. The relative bias (equation 2) is the absolute bias normalized by the square root of the mean of the product of observed and simulated flow speed. The root mean square error (RMSE, equation 3) is the square root of the quadratic mean of differences between simulated and observed velocities. It adds to the bias as a measure of random deviation and indicates the accuracy of simulations. The Hanna & Heinold index (HH, equation 4, Hanna and D., 1985) normalized the RMSE by the mean of the product of the observed and simulated flow speed. It indicates the relative uncertainty from the mean flow and avoids biasing when the model underestimates the currents (negative bias, Mentaschi et al., 2013). The scatter index (SI, equation 5) is the quadratic mean of the difference between simulated and observed flow speed fluctuations around the mean, normalized by the mean of the product of observed and simulated flow speed. It indicates if the simulated flow speed fluctuates more or less around the mean than the observed flow speed. The correlation index (equation 6) is the product of simulated and observed fluctuations around the mean flow speed, normalized by the product of the standard deviation of the simulated and observed flow speed. It varies between -1 and +1. Values close to 1 indicate co-variation (-1 indicates opposed variation) in the dynamics of simulated and observed flow speed, while values close to 0 indicate the dynamics of simulated and observed flow are different.

2.5. Definition of the reference period and the three types of specific events

In order to separate uncertainties due to model implementation and hypothesis violation, the six indicators were assessed separately during reference periods defined by low wind conditions, no swell and absence of significant stratification, and during events with either strong wind conditions (turbulence closure or atmospheric forcing reliability), swell (hydrostatic hypothesis violation), or in stratified conditions (Boussinesq approximation violation). Importantly, the indicators were integrated over a same duration during reference periods as the event duration.

Wind conditions over the entire Gulf of Lion were estimated using the wind stress used to force the ocean circulation simulations at the closest atmospheric model grid point from the Planier and POEM stations (Figure 1). Low and strong wind conditions correspond to wind speed lower than 40 km/hr and larger than 50 km/hr, respectively, separating negligible effects from significant impacts in Beaufort scale. Wind speed thresholds were converted into wind stress values to be detected in the atmospheric forcings (using $\tau = C_D \rho U^2$ with τ the wind stress in Pa, U the wind speed in m.s^{-1}, C_D a drag coefficient of 0.00171 and ρ the air density of 1.225 kg/m^3, according to Smith, 1988). Practically, during the reference period, wind stress values should not exceed 0.2586 Pa at both Planier and POEM stations, while wind events were defined by wind stress values larger than 0.4041 Pa during more than 12 hr at both stations. Numerous northerly wind events (37, Figure 2) were detected with wind stresses between 0.6903 Pa and 2.4939 Pa, as expected in the Gulf of Lion (Guénard et al., 2005). These events were grouped according to their duration into four different

classes (12-24 hr, 24-36 hr, 36-48 hr, 48-60 hr, appendix Figure A.1).

Wave conditions over the entire Gulf of Lion were assessed using observations over the period January 2010- June 2013 at four stations (Banyuls, Espiguette, Leucate, Sète, Figure 1) of the In Situ National Data Archiving Center of Waves (Centre d'Archivage National des Données de Houle In Situ, http://candhis.cetmef.developpement-durable.gouv.fr, accessed 01/06/2021). Wave events were defined as the occurrence of swell with a peak period larger than 8 s, a significant period larger than 5 s and a zeroth order moment wave height larger than 3 m at any of four stations during at least 12 hours. The four stations were necessary to detect the southerly to easterly swell impacting the Gulf of Lion (Guizien, 2009). Such swell with wave length larger than the resolution of the flow model at the coast ($\sim$ 100 m) exhibit wave steepness (wave heigth to wave length ratio) larger than 1%, which corresponded to vertical to horizontal velocity ruling out the hydrostatic assumption of the flow model. These criteria resulted in the selection of five swell events with different durations: 12 hr (max.: Tp=12.5 s, Tz=8.0 s, Hm0=4.2 m), 15 hr (max.: Tp=11.8 s, Tz=8.0 s, Hm0=5.5 m), 21 hr (max.: Tp=10.5 s, Tz=8.3 s, Hm0=4.1 m), 40 hr (max.: Tp=10.5 s, Tz=7.8 s, Hm0= 5.6 m) and 86 hr (max.: Tp=10.5 s, Tz=7.7 s, Hm0=4.4 m) (Figure 2). On the contrary, the reference period was defined by the absence of swell with the above mention characteristics at the four stations.

Stratification was estimated at each station after computing the Brunt-Väisälä frequency $N^2(z) = -g/\rho_0 d\rho_0/dz$ with g the gravitational acceleration, ρ_0 the density of sea water and z the depth in the sea water using simulated salinity and temperature profiles to calculate sea water density

(Fofonoff and Millard, 1983). The threshold to separate stratified and unstratified periods was the maximum value of the Brunt-Väisälä frequency over the entire water column of 0.005 s^{-2} for at least 12 hours. This value was defined according to Gill (1982). This allowed us to assess the stratification events at each station separately. No stratification events were detected at the stations SOLA, LD, Lion and Planier, while at Mesurho, which was closest to the Rhône river, the water column was almost always stratified. Since at the aforementioned stations, there was either an absence of stratification events or of reference conditions, there could be no comparison between the two. Therefore, none of these stations were used for testing the effect of the Boussinesq hypothesis violation on the model's performance. The only stations that were considered were BeSete and POEM (shallow stations) with four stratification events of 249 hr (max. N^2=0.0150 s^{-2}), 81 hr (max. N^2=0.0084 s^{-2}), 194 hr (max. N^2= 0.0202 s^{-2}) and 143 hr (max. N^2=0.0124 s^{-2}) at BeSete and three stratification events of 74 hr (max. N^2=0.0953 s^{-2}), 79 hr (max. N^2=0.0310 s^{-2}) and 103 hr (max. N^2=0.0211 s^{-2}) at POEM (Figure 2).

The three types of events were decorrelated and wind events could happen any time in the year (Figure 2). Therefore, reference periods were not separated according to the season.

2.6. Assessment of model performance during specific events

Each of the aforementioned indicators is expected to vary with the duration, the moment and the location on which they were calculated, either randomly or systematically. Systematic variation indicates a worse model performance. To test the model's performance under specific conditions (such

as strong wind, waves or density stratification), the value of each of these indicators was computed during and in absence of such conditions over a same duration. To compare the events to the reference period, reference cumulative frequency distributions (CFDs) were established for each indicator and each station for the same duration as the event to test. To do so, a set of 200 time periods with an equal event duration as the event to test was randomly selected out of the reference period and used to build this reference CFD for the indicator. These 200 time periods each had unique starting moments, but in the case of stations with a short observation period, overlap is possible. A bootstrap procedure was applied to produce 250 repeats of the reference CFD. Those repeats were used to estimate the most probable reference frequency distribution and a confidence interval around it. The most probable reference CFD for the indicator was thus defined by the 50% quartile (median) of the 250 repeats. For the wave and stratification events, the reference CFDs were calculated using the same duration as the event to test. For the wind events, the reference CFD was calculated over a duration equal to the duration of the middle of the class this event belonged to (e.g A wind event of 14 hr would belong to the class of 12-24hr and be compared to the CFD calculated over 18 hr, as this is the middle of the class, see appendix Figure A.2 for more information. Reference CFDs were used to determine the corresponding cumulative frequencies of each indicator/station/event by assessing the event's indicator value compared to the reference CFD (Figure 3, additional schematic in appendix Figure A.2). Those corresponding cumulative frequencies were used to assess the model's performance, by comparing its value to a threshold value. For RMSE, HH and SI and relative

bias, if the corresponding cumulative frequency of the indicator value during the event was larger than 75%, it was considered to have a higher uncertainty during the event. For the correlation, the uncertainty of the model is the lowest when the correlation is closer to 1. Therefore, there was a bad model performance when the corresponding cumulative frequency was less than 25%. For the bias, the uncertainty is the lowest when bias is close to zero. Therefore, bad model performance was determined by a corresponding cumulative frequency below 12.5% or above 87.5%. The proportion of events during which the model performed worse than during the reference period was calculated per station, per indicator and per event type. Those proportions were averaged across all indicators and stations to assess whether there was a difference in model performance per station, indicator or event type.

3. Results

The reference period CFD of each accuracy indicator in absence of wind, waves and stratification was computed for durations ranging from 12 hr to 249 hr at each station (Figure 4 for a duration of 42 hr). Overall, the simulated flow speed was underestimated at deep stations during the reference period, with bias median values calculated over 42 hr ranging from -3 cm/s at Lion to -1.2 cm/s in Creus and LD (Figure 4A). At the shallow stations, the flow speed could be either underestimated (BeSete and SOLA, bias median values of -1.2 cm/s and -0.6 cm/s resp.) or overestimated (Mesurho and POEM, bias median values of 3.6 cm/s and 0.6 cm/s; Figure 4A). In both groups of stations, bias values spread was large, with the first and third quartile being -5.4 and 0 cm/s at deep stations and -4.2 and 6.6 cm/s at shallow stations.

After normalizing by the current magnitude in each station, the relative bias was smaller at the shallow stations (with median values ranging from 30% at BeSete and SOLA to 40% at POEM) than at the deep stations (with median values ranging from 35% at Creus to 85% at Lion, Figure 4B). The relative scatter index (SI) was variable amongst the stations, with a similar variability among deep and shallow stations (median values ranging from 65% at Lion to 93% at Mesurho; Figure 4C). As a result, the HH indicator, which combines the relative scatter and relative bias was larger at deep stations (median values ranging from 95% at LD and Creus to 110% at Lion) than at shallow stations (median values ranging from 75% at SOLA and BeSete to 83% at Mesurho, Figure 4E). Noteworthy, the median HH values were larger than 70% at all stations. In absolute values, the median RMSE was similar at deep and shallow stations, ranging from 2.5 cm/s at Planier and BeSete to 5.6 cm/s at Creus and 5.3 cm/s at Mesurho (Figure 4D). However, the RMSE's third quartile was less homogenous across deep stations, which had values ranging from 3.2 cm/s to 12.6 cm/s, than across shallow stations, with values ranging from 3.2 cm/s to 6.7 cm/s. Although the correlation was low at all stations, it was higher at the shallow stations than at the deep stations (Figure 4F). Median (third quartile) values ranged from 0.03 (0.14, resp.) at BeSete to 0.13 (0.23, resp.) at POEM while median values in deep stations had a median of -0.01 for LD and Lion and were always less than 0.01. Although the CFDs of the accuracy indicators clustered according to the duration of the event, the deviation between the CFDs calculated over 12-24 hr and those calculated over more than 72 hr remained limited (Appendix Figure A.3). The median correlation at BeSete varied between 0.02 and 0.06

and the maximum between 0.33 and 0.63 for integration duration increasing from 12-24 hr to more than 72 hr (Figure 5). While the correlation and bias (relative and absolute) improved with increasing integration duration, the SI worsened. With increasing integration duration, the deviation between the first and third quartile of the RMSE and HH indicators decreased and the median value increased (Figure 5 for the correlation, appendix Figure A.3 for the other indicators at BeSete). Despite the fact that the CFDs of the accuracy indicators calculated during the reference period varied with the event duration, the corresponding cumulative frequencies of the correlation indicator calculated during wind, wave or stratification events were not tied to the duration of the events, regardless of the station (Figure 6 for wind events). Overall, the proportion of events where the model performed worse during the events than during the reference period was low no matter the event type. The average ratio worse ranged from 25% for the wind events to 35% for the wave events (Table 2, Table 3). For the stratification events, which were only studied at BeSete and POEM, the model performed worse during the events than during the reference period for 25% and 33% of the events on average, respectively (Table 4). However, the assessment of the model's performance varied greatly depending on the indicator, with the HH indicating a 13% ratio worse and the RMSE showing a 45% ratio worse in the wind events for instance (Table 2, Figure 7B). When comparing the model's performance across event types and stations, it was worse during wave events than during wind events at shallow stations (except at the Mesurho station in front of the Rhone River mouth), while no trend could be observed at deep stations (Figure 7A). During the wave events, the model performed

similarly across all stations, with all stations indicating that the model was worse than during the reference period less than 33% of the time on average, except at the POEM station, where the ratio worse reached 67% (Table 3). During the wind events, the model performed slightly better at the shallow stations (ratio worse ranging from 11% to 31%) than at the deep stations (ratio worse ranging from 26% to 37%, Table 2). For both event types, absolute indicators (RMSE and bias) displayed worse model performance than relative indicators (Figure 7B). All indicators except SI displayed worse model performance during wave events than during wind events (Figure 7B).

4. Discussion

The present study quantified various indicators to describe the deviation between observed and simulated flow speed across shallow and deep stations within a highly dynamic region, during and outside short term events of three types (wind, waves, stratification).

The assessment of ocean model accuracy has largely been implemented by comparing simulated and observed hydrological variables (temperature and salinity; e.g. Gustafsson et al., 1998; Reffray et al., 2004; André et al., 2005; Kara et al., 2006; Chelton et al., 2007; Pairaud et al., 2011; Renault et al., 2012; Marzocchi et al., 2015; Seyfried et al., 2017; Akhtar et al., 2018) as their dynamics integrates transport (velocity) and mixing (turbulent kinetic energy) in ocean circulation models. However, hydrological variables are little informative about transport and mixing when well-mixed conditions prevail, which is often the case in coastal areas (Gill, 1982; Holt et al., 2009).

The ability of the SYMPHONIE model to simulate flow speed and not

only hydrological parameters in the Gulf of Lion has been assessed before but only qualitatively under a variety of coastal processes, such as thermally stratified conditions (Petrenko et al., 2005), fresh water mixing in the Rhône River prodelta (Estournel et al., 2001), wind driven Eckman flow (Davies et al., 1998; Lapouyade and Durrieu De Madron, 2001; Molcard et al., 2002; Schaeffer et al., 2011; Estournel et al., 2016), swell events (Michaud et al., 2012; Mikolajczak et al., 2020) and dense water cascading (Ulses et al., 2008; Estournel et al., 2016). Only one study assessed quantitatively the uncertainty on simulated speeds in the Gulf of Lion. It compared another SYMPHONIE configuration than the one of the present study (horizontal resolution ranging from 300 m to 7 km, with and without wave coupling) to part of the dataset used in our study that is a two month period which included several wave events in (February to March, 2011, Mikolajczak, 2019). The bias was 4 cm/s at the Mesurho station and -4 cm/s at the POEM station whilst the RMSEs were 10 cm/s and 8 cm/s, respectively. The present study compliments previous assessments of the SYMPHONIE model in the Gulf of Lion, whilst extending them in space and time and using six quantitative indicators. Using data from multiple years and stations, particularly shallow versus deep ones enabled us to assess model implementation uncertainties in the present study configuration. Focussing first on a reference period (unstratified, with low wind conditions and no wave), when model assumptions are expected to be valid, bias and RMSE on simulated speeds during the reference period were larger than the measuring device accuracy (about 1 cm/s Instruments, 2007). This is generally the the case among the few studies that quantified uncertainties on simulated speeds, elsewhere. While

comparing Glazur60 simulations of the NEMO model (horizontal resolution of 1/64° hence 1.3 to 1.7 km) to the data of a fixed ADCP mooring located at a hundred meters depth in the eastern part of the Gulf of Lion, a bias of 3.5 cm/s at 90 m and 7 cm/s at 20 m depth was found between simulations and observations over an 11 month integration period (Barrier et al., 2016). Similarly, while evaluating the effect of boundary conditions on simulations using the SoFLA-HYCOM model configuration (1/25° hence 3.5 to 4 km horizontal resolution) at shallow stations around the Strait of Florida, the mean bias and the RMSE calculated between simulations and observations over a one year period ranged from -3.5 cm/s to 8.2 cm/s for the bias and from 5 to 13 cm/s for the RMSE, depending on the model's configuration and the station (Kourafalou et al., 2009). Despite flow speed simulations not being as precise as ADCP measurements, it is remarkable that the present study's bias and RMSE values were smaller than the values reported in those quantitative studies, despite these indicators were calculated over longer periods in the latter studies than in our study (weeks versus days). Indeed, the systematic bias and the RMSE are expected to decrease with increasing integration duration (Dekking, 2005). However, comparing bias and RMSE values between simulations and observations in different environments can be misleading regarding model performance and relative indicators should be used.

In the present study, lower relative bias and HH were found at shallow stations compared to deep ones. The better model performance at the shallow stations could be due to the refinement of the horizontal spatial resolution, thanks to the adaptive resolution of the curvilinear grid. Increasing

the resolution of model configurations have been tested to improve agreement with other types of observations than flow speeds, sometimes showing predictions improvements (Thoppil et al., 2011; Kirtman et al., 2012; Putman and He, 2013; Ringler et al., 2013; Akhtar et al., 2018; Kvile et al., 2018; Ridenour et al., 2019). In addition to relative bias which indicates goodness of transport predictions, the present study evaluated the correlation between simulated and observed flow speed, an indicator generally disregarded. At all stations, correlation indicated that the simulation failed to reproduce the short term flow dynamics (hours to days). Short term flow dynamics is expected to be driven by atmospherical forcings, especially in the Gulf of Lion, where coastal circulation simulations have been shown to dramatically change with the wind's spatial gradient (Dumas and Langlois, 20O9). Hence, the present study simulations were driven by atmospheric field outputs from a reanalysis with assimilated observations and was updated every three hours at the finest resolution available for the area at the time of the simulations (Hamon et al., 2016). One way to improve the simulations' accuracy is to use the bidirectional atmospheric coupling technique (Gustafsson et al., 1998; Chelton et al., 2007; Schaeffer et al., 2011; Akhtar et al., 2018). Two-ways air-sea coupling performed better than one-way atmospheric forcing during autumn storms, when the sea surface cools rapidly (Seyfried et al., 2017). Nevertheless, in the Gulf of Lion, the added value of coupling atmosphere-ocean simulations on modelled wind speed intensity and sea surface temperature was not significant (Renault et al., 2012). Interestingly, in the present study, the indicators did not display a worse model performance during strong wind events when atmosphere-ocean interaction

increased, than outside those events. In any case, this limitation to reproduce the short term flow dynamics, including in low wind conditions, raises the question of how short term (days) velocity dynamics' inaccuracies alter particle tracking simulations (e.g. used in larval dispersal studies, Briton et al., 2018).

Similarly, the model's performance was not systematically worse during wave events, although it was slightly worse during wave than during wind events. When comparing a hydrostatic, quasi-hydrostatic and nonhydrostatic model, no difference between the three models was found at large scales with coarse resolution (1° horizontal resolution, Marshall et al., 1997). However, it is expected that quasi-hydrostatic and nonhydrostatic models should be preferred when the spatial resolution increases as in the present study simulations (Magaldi and Haine, 2015). Incorporating the effects of waves on the coastal circulation simulations has been considered previously in the Gulf of Lion and flow speed simulations in the surf zone (0-15m water depth) were improved by using a fully nonhydrostatic coupled current-wave model (Michaud et al., 2012). However, outside the surfzone, deviations between observed and simulated flow speeds at POEM and Mesurho (same location as in the present study but another time period) were similar regardless of wave forcing.

Another model assumption which could have altered the model's performance is the Boussinesq approximation, which can be violated in thermal or fresh water stratification. In the Gulf of Lion, stratification effect was only studied qualitatively. During summer, incorrect representation of the stratification in the Gulf of Lion led to a misplacement of the NC in the

simulations compared to the field observations (Petrenko et al., 2005). In contrast, simulations of the Rhône plume compared to radar observations showed that the SYMPHONIE model can reproduce the spatial variation of the current in front of the river mouth outside of strong wind events (Estournel et al., 2001). Comparing with the rare quantitative studies from other areas is equally unconclusive as only absolute indicators were computed (bias (4-15cm/s) and RMSE (6-18cm/s) over two week period of salinity stratification in an estuary in the USA Yang and Khangaonkar, 2009). In the present study, testing model performance alteration due to stratification was limited to few fresh water input events in two stations only as in other stations, the water column was either never or always stratified. In these few events, model performance was not significantly worse. However, outside specific events, indicators were systematically larger at the continuously stratified Mesurho station than at the other shallow stations, suggesting stratification effect should be further tested.

In conclusion, a quantitative validation of simulated current speeds was performed over a three-year period using in situ flow speed observations from eight fixed moorings (four shallow and four deep). Multiple absolute, and more importantly, relative indicators were calculated to evaluate the performance of the model. In absence of wind, wave or stratification events, the model performed better at shallow stations than at deep stations in predicting the mean flow speed (lower relative bias). In contrast, scatter index was equally large at all stations and correlation over short duration periods was always low, indicating discrepancies between simulated and observed flow speed dynamics. Overall, the model did not perform notably worse during

wind, wave or stratified events than outside of events. However, the model's performance was lower during wave events than during wind events at shallow stations.

5. Acknowledgements

Some current observations were obtained within the framework of the French national observation services MOOSE (https://www.moose-network.fr/) and COAST-HF (https://coast-hf.fr/). Wave data were provided by the Centre d'études et d'expertise sur les risques, l'environnement, la mobilité et l'aménagement, the Direction Régionale de l'environnement de l'aménagement et du logement of the Occitanie region and the Observatoire Océanologique de Banyuls (https://candhis.cerema.fr/).

References

Akhtar, N., Brauch, J., Ahrens, B., 2018. Climate modeling over the Mediterranean Sea: impact of resolution and ocean coupling. Climate Dynamics 51, 933–948. URL: http://link.springer.com/10.1007/s00382-017-3570-8, doi:10.1007/s00382-017-3570-8.

Aloisi, J.C., Got, H., Monaco, A., 1973. Carte géologique du précontinent languedocien au 1/250000ième. International Institute for Aerial Survey and Earth Sciences .

André, G., Garreau, P., Garnier, V., Fraunié, P., 2005. Modelled variability of the sea surface circulation in the North-western Mediter-

ranean Sea and in the Gulf of Lions. Ocean Dynamics 55, 294–308. URL: http://link.springer.com/10.1007/s10236-005-0013-6, doi:10.1007/s10236-005-0013-6.

Barrier, N., Petrenko, A.A., Ourmières, Y., 2016. Strong intrusions of the Northern Mediterranean Current on the eastern Gulf of Lion: insights from in-situ observations and high resolution numerical modelling. Ocean Dynamics 66, 313–327. URL: http://link.springer.com/10.1007/s10236-016-0921-7, doi:10.1007/s10236-016-0921-7.

Bentsen, M., Evensen, G., Drange, H., Jenkins, A.D., 1999. Coordinate Transformation on a Sphere Using Conformal Mapping. Monthly Weather Review 127, 2733–2740. URL: http://journals.ametsoc.org/doi/10.1175/1520-0493(1999)127<2733:CTOASU>2.0.CO;2, doi:10.1175/1520-0493(1999)127¡2733:CTOASU¿2.0.CO;2.

Bourrin, F., Many, G., Durrieu de Madron, X., Martín, J., Puig, P., Houpert, L., Testor, P., Kunesch, S., Mahiouz, K., Béguery, L., 2015. Glider monitoring of shelf suspended particle dynamics and transport during storm and flooding conditions. Continental Shelf Research 109, 135–149. URL: https://linkinghub.elsevier.com/retrieve/pii/S0278434315300509, doi:10.1016/j.csr.2015.08.031.

Boussinesq, J., 1903. Théorie analytique de la chaleur mise en harmonie avec la thermodynamique et avec la théorie mécanique de la lumière: Refroidissement et échauffement par rayonnement, conductibilité des tiges,

583 lames et masses cristallines, courants de convection, théorie. Gauthiers-
584 Villars.

585 Briton, F., Cortese, D., Duhaut, T., Guizien, K., 2018. High-
586 resolution modelling of ocean circulation can reveal retention
587 spots important for biodiversity conservation. Aquatic Conser-
588 vation: Marine and Freshwater Ecosystems 28, 882–893. URL:
589 https://onlinelibrary.wiley.com/doi/10.1002/aqc.2901,
590 doi:10.1002/aqc.2901.

591 Cai, X., Zhang, Y.J., Shen, J., Wang, H., Wang, Z., Qin, Q.,
592 Ye, F., 2020. A Numerical Study of Hypoxia in Chesapeake
593 Bay Using an Unstructured Grid Model: Validation and Sensi-
594 tivity to Bathymetry Representation. JAWRA Journal of the
595 American Water Resources Association , 1752–1688.12887URL:
596 https://onlinelibrary.wiley.com/doi/10.1111/1752-1688.12887,
597 doi:10.1111/1752-1688.12887.

598 Chassignet, E.P., Hurlburt, H.E., Smedstad, O.M., Halliwell, G.R.,
599 Hogan, P.J., Wallcraft, A.J., Baraille, R., Bleck, R., 2007.
600 The HYCOM (HYbrid Coordinate Ocean Model) data assim-
601 ilative system. Journal of Marine Systems 65, 60–83. URL:
602 https://linkinghub.elsevier.com/retrieve/pii/S0924796306002855,
603 doi:10.1016/j.jmarsys.2005.09.016.

604 Chelton, D.B., Schlax, M.G., Samelson, R.M., 2007. Summertime Cou-
605 pling between Sea Surface Temperature and Wind Stress in the Cal-
606 ifornia Current System. Journal of Physical Oceanography 37, 495–

517. URL: http://journals.ametsoc.org/doi/10.1175/JPO3025.1, doi:10.1175/JPO3025.1.

Clark, P.U., Pisias, N.G., Stocker, T.F., Weaver, A.J., 2019. The role of the thermohaline circulation in abrupt climate change. encyclopedia of ocean sciences, in: Encyclopedia of Ocean Sciences. Elsevier, pp. 405–411. URL: https://linkinghub.elsevier.com/retrieve/pii/B9780124095489116252, doi:10.1016/B978-0-12-409548-9.11625-2.

Cowen, R.K., Lwiza, K.M.M., Sponaugle, S., Paris, C.B., Olson, D.B., 2000. Connectivity of Marine Populations: Open or Closed? Science 287, 857–859. URL: https://www.science.org/doi/10.1126/science.287.5454.857, doi:10.1126/science.287.5454.857.

Davies, A.M., Kwong, S.C., Flather, R.A., 1998. A three-dimensional model of wind-driven circulation on the shelf. Continental Shelf Research 18, 289–340. URL: https://linkinghub.elsevier.com/retrieve/pii/S0278434397000605, doi:10.1016/S0278-4343(97)00060-5.

Dekking, M. (Ed.), 2005. A modern introduction to probability and statistics: understanding why and how. Springer texts in statistics, Springer, London.

Dohan, K., Dohan, K., Dohan, K., Dohan, K., Dohan, K., Dohan, K., Dohan, K., Dohan, K., Dohan, K., Dohan, K., 2010. Measuring the Global Ocean Surface Circulation with Satellite and In Situ Observations, in: Proceedings of OceanObs'09: Sustained Ocean Ob-

servations and Information for Society, European Space Agency. pp. 237–248. URL: http://www.oceanobs09.net/proceedings/cwp/cwp23, doi:10.5270/OceanObs09.cwp.23.

Drévillon, M., Bahurel, P., Bazin, D., Benkiran, M., Beuvier, J., Crosnier, L., Drillet, Y., Durand, E., Fabardines, M., Garcia Hermosa, I., Giordan, C., Gutknecht, E., Hernandez, F., Chune, S., Le Traon, P.Y., Lellouche, J.M., Levier, B., Melet, A., Obaton, D., Paul, J., Peltier, M., Peyrot, D., Rémy, E., von Schuckmann, K., Thomas-Courcoux, C., 2018. Learning about Copernicus Marine Environment Monitoring Service "CMEMS": A Practical Introduction to the Use of the European Operational Oceanography Service, in: Chassignet, E.P., Pascual, A., Tintoré, J., Verron, J. (Eds.), New Frontiers in Operational Oceanography. GODAE OceanView. URL: http://purl.flvc.org/fsu/fd/FSU$_l$ibsubv1$_s$cholarship$_s$ubmission$_1$536248237$_d$2400064, doi : 10.17125/gov2018.ch25.$Dufois, F., Garreau, P., Le\ Hir, P., Forget, P.$, 2008.$Wave-$ $andcurrent-inducedbottomshearstressdistributionintheGulfofLions.ContinentalShelfRese$ $-1934.URL$: https://linkinghub.elsevier.com/retrieve/pii/S0278434308001283, doi : 10.1016/$j.csr$.2008.03.028.

Dulière, V., Gypens, N., Lancelot, C., Luyten, P., Lacroix, G., 2019. Origin of nitrogen in the English Channel and Southern Bight of the North Sea ecosystems. Hydrobiologia 845, 13–33. URL: http://link.springer.com/10.1007/s10750-017-3419-5, doi:10.1007/s10750-017-3419-5.

Dumas, F., Langlois, G., 20O9. Mars model for applications at regional scale. scientific model description. URL:

https://mars3d.ifremer.fr/docs/$_{s}tatic/2009_1 1_2 2_{D}ocMARS_{G}B.pdf.DurrieuDe\ Madron, X$
https://www.seanoe.org/data/00349/45980/, *doi* :
10.17882/45980.*type* : *dataset*.

Estournel, C., 2003. Observation and modeling of the winter coastal oceanic circulation in the Gulf of Lion under wind conditions influenced by the continental orography (FETCH experiment). Journal of Geophysical Research 108, 8059. URL: http://doi.wiley.com/10.1029/2001JC000825, doi:10.1029/2001JC000825.

Estournel, C., Broche, P., Marsaleix, P., Devenon, J.L., Auclair, F., Vehil, R., 2001. The Rhone River Plume in Unsteady Conditions: Numerical and Experimental Results. Estuarine, Coastal and Shelf Science 53, 25–38. URL: https://linkinghub.elsevier.com/retrieve/pii/S0272771400906851, doi:10.1006/ecss.2000.0685.

Estournel, C., Testor, P., Damien, P., D'Ortenzio, F., Marsaleix, P., Conan, P., Kessouri, F., Durrieu de Madron, X., Coppola, L., Lellouche, J., Belamari, S., Mortier, L., Ulses, C., Bouin, M., Prieur, L., 2016. High resolution modeling of dense water formation in the north-western Mediterranean during winter 2012–2013: Processes and budget. Journal of Geophysical Research: Oceans 121, 5367–5392. URL: https://onlinelibrary.wiley.com/doi/abs/10.1002/2016JC011935, doi:10.1002/2016JC011935.

Falkowski, P.G., Barber, R.T., Smetacek, V., 1998. Biogeochemical Controls and Feedbacks on Ocean Primary Production. Science 281, 200–206. URL:

https://www.science.org/doi/10.1126/science.281.5374.200, doi:10.1126/science.281.5374.200.

Fisher, A.W., Sanford, L.P., Scully, M.E., 2018. Wind-Wave Effects on Estuarine Turbulence: A Comparison of Observations and Second-Moment Closure Predictions. Journal of Physical Oceanography 48, 905–923. URL: https://journals.ametsoc.org/view/journals/phoc/48/4/jpo-d-17-0133.1.xml, doi:10.1175/JPO-D-17-0133.1.

Fofonoff, N.P., Millard, R.C., 1983. Algorithms for computation of fundamental properties of seawater. UNESCO Technical Papers in Marine Science 44(53). URL: http://darchive.mblwhoilibrary.org:8080/handle/1912/2470.

Gentil, M., Many, G., Durrieu de Madron, X., Cauchy, P., Pairaud, I., Testor, P., Verney, R., Bourrin, F., 2020. Glider-Based Active Acoustic Monitoring of Currents and Turbidity in the Coastal Zone. Remote Sensing 12, 2875. URL: https://www.mdpi.com/2072-4292/12/18/2875, doi:10.3390/rs12182875.

Gill, A.E., 1982. Atmosphere–Ocean Dynamics. Academic Press, New York.

Guizien, K., 2009. Spatial variability of wave conditions in the gulf of lions (nw mediterranean sea). Life and Environment 59, 261–270. URL: https://www.researchgate.net/publication/250306276.

Guizien, K., Barthélemy, E., Inall, M.E., 1999. Internal tide generation at a shelf break by an oblique barotropic tide: Observations and analytical modeling. Journal of Geophysical Research: Oceans 104,

15655–15668. URL: http://doi.wiley.com/10.1029/1999JC900089, doi:10.1029/1999JC900089.

Guizien, K., Charles, F., Lantoine, F., Naudin, J.J., 2007. Nearshore dynamics of nutrients and chlorophyll during Mediterranean-type flash-floods. Aquatic Living Resources 20, 3–14. URL: http://www.alr-journal.org/10.1051/alr:2007011, doi:10.1051/alr:2007011.

Gustafsson, N., Nyberg, L., Omstedt, A., 1998. Coupling of a High-Resolution Atmospheric Model and an Ocean Model for the Baltic Sea. Monthly Weather Review 126, 2822–2846. URL: http://journals.ametsoc.org/doi/10.1175/1520-0493(1998)126<2822:COAHRA>2.0.CO;2, doi:10.1175/1520-0493(1998)126¡2822:COAHRA¿2.0.CO;2.

Guénard, V., Dobrinski, P., Caccia, J., Campistron, B., Benech, B., 2005. An observational study of the mesoscale mistral dynamics. Boundary Layer Meteorology 115, 263–288.

Hamon, M., Beuvier, J., Somot, S., Lellouche, J.M., Greiner, E., Jordà, G., Bouin, M.N., Arsouze, T., Béranger, K., Sevault, F., Dubois, C., Drevillon, M., Drillet, Y., 2016. Design and validation of MEDRYS, a Mediterranean Sea reanalysis over the period 1992–2013. Ocean Science 12, 577–599. URL: https://os.copernicus.org/articles/12/577/2016/, doi:10.5194/os-12-577-2016.

Hanna, S., D., H., 1985. Development and application of a simple method for evaluating air quality models. American Petroleum Institute 4409.

Holt, J., Harle, J., Proctor, R., Michel, S., Ashworth, M., Batstone, C., Allen, I., Holmes, R., Smyth, T., Haines, K., Bretherton, D., Smith, G., 2009. Modelling the global coastal ocean. Philosophical Transactions of the Royal Society A: Mathematical, Physical and Engineering Sciences 367. URL: https://royalsocietypublishing.org/doi/10.1098/rsta.2008.0210, doi:10.1098/rsta.2008.0210.

Hu, Z., Doglioli, A., Petrenko, A., Marsaleix, P., Dekeyser, I., 2009. Numerical simulations of eddies in the Gulf of Lion. Ocean Modelling 28, 203–208. URL: https://linkinghub.elsevier.com/retrieve/pii/S1463500309000237, doi:10.1016/j.ocemod.2009.02.004.

Hu, Z., Petrenko, A., Doglioli, A., Dekeyser, I., 2011. Study of a mesoscale anticyclonic eddy in the western part of the Gulf of Lion. Journal of Marine Systems 88, 3–11. URL: https://linkinghub.elsevier.com/retrieve/pii/S0924796311000376, doi:10.1016/j.jmarsys.2011.02.008.

Instruments, R., 2007. Accoustic Doppler Current Profiler Technical Manual. Technical Report P/N 957-6150-00. Teledyne.

James, I., 2002. Modelling pollution dispersion, the ecosystem and water quality in coastal waters: a review. Environmental Modelling & Software 17, 363–385. URL: https://linkinghub.elsevier.com/retrieve/pii/S1364815201000809, doi:10.1016/S1364-8152(01)00080-9.

727 Kara, A.B., Barron, C.N., Martin, P.J., Smedstad, L.F., Rhodes, R.C.,
728 2006. Validation of interannual simulations from the 1/8° global Navy
729 Coastal Ocean Model (NCOM). Ocean Modelling 11, 376–398. URL:
730 https://linkinghub.elsevier.com/retrieve/pii/S1463500305000132,
731 doi:10.1016/j.ocemod.2005.01.003.

732 Kirtman, B.P., Bitz, C., Bryan, F., Collins, W., Dennis, J., Hearn,
733 N., Kinter, J.L., Loft, R., Rousset, C., Siqueira, L., Stan, C.,
734 Tomas, R., Vertenstein, M., 2012. Impact of ocean model resolu-
735 tion on CCSM climate simulations. Climate Dynamics 39, 1303–
736 1328. URL: http://link.springer.com/10.1007/s00382-012-1500-3,
737 doi:10.1007/s00382-012-1500-3.

738 Kourafalou, V.H., Peng, G., Kang, H., Hogan, P.J., Smedstad, O.M.,
739 Weisberg, R.H., 2009. Evaluation of Global Ocean Data Assimila-
740 tion Experiment products on South Florida nested simulations with
741 the Hybrid Coordinate Ocean Model. Ocean Dynamics 59, 47–
742 66. URL: http://link.springer.com/10.1007/s10236-008-0160-7,
743 doi:10.1007/s10236-008-0160-7.

744 Kvile, K., Romagnoni, G., Dagestad, K.F., Langangen, , Kristiansen,
745 T., 2018. Sensitivity of modelled North Sea cod larvae transport to
746 vertical behaviour, ocean model resolution and interannual variation in
747 ocean dynamics. ICES Journal of Marine Science 75, 2413–2424. URL:
748 https://academic.oup.com/icesjms/article/75/7/2413/4975493,
749 doi:10.1093/icesjms/fsy039.

750 Lapouyade, A., Durrieu De Madron, X., 2001. Seasonal variability of the

advective transport of particulate matter and organic carbon in the Gulf of Lion (NW Mediterranean). Oceanologica Acta 24, 295–312. URL: https://linkinghub.elsevier.com/retrieve/pii/S0399178401011483, doi:10.1016/S0399-1784(01)01148-3.

Lazure, P., Dumas, F., 2008. An external–internal mode coupling for a 3D hydrodynamical model for applications at regional scale (MARS). Advances in Water Resources 31, 233–250. URL: https://linkinghub.elsevier.com/retrieve/pii/S0309170807001121, doi:10.1016/j.advwatres.2007.06.010.

Le Provost, C., Lyard, F.H., 2000. How can we improve a global ocean tide model at a regional scale? a test on the yellow sea and the east china sea. Journal of geophysical research 105, 8707–8725.

Ludwig, W., Dumont, E., Meybeck, M., Heussner, S., 2009. River discharges of water and nutrients to the Mediterranean and Black Sea: Major drivers for ecosystem changes during past and future decades? Progress in Oceanography 80, 199–217. URL: https://linkinghub.elsevier.com/retrieve/pii/S0079661109000020, doi:10.1016/j.pocean.2009.02.001.

Mader, J., Rubio, A., Novellino, A., Alba, M., Corgnati, L., Mantovani, C., Griffa, A., Gorringe, P., Fernandez, V., 2016. The European HF Radar inventory. Technical Report. EuroGOOS publications.

Magaldi, M.G., Haine, T.W., 2015. Hydrostatic and non-hydrostatic simulations of dense waters cascading off a shelf: The East Greenland case. Deep

774 Sea Research Part I: Oceanographic Research Papers 96, 89–104. URL:
775 https://linkinghub.elsevier.com/retrieve/pii/S0967063714001915,
776 doi:10.1016/j.dsr.2014.10.008.

777 Mannarini, G., Carelli, L., 2019. VISIR-I.b: waves
778 and ocean currents for energy efficient navigation.
779 preprint. Earth and Space Science Informatics. URL:
780 https://gmd.copernicus.org/preprints/gmd-2018-292/gmd-2018-292.pdf,
781 doi:10.5194/gmd-2018-292.

782 Mansui, J., Darmon, G., Ballerini, T., van Canneyt, O., Ourmieres, Y.,
783 Miaud, C., 2020. Predicting marine litter accumulation patterns in
784 the Mediterranean basin: Spatio-temporal variability and compari-
785 son with empirical data. Progress in Oceanography 182, 102268. URL:
786 https://linkinghub.elsevier.com/retrieve/pii/S0079661120300069,
787 doi:10.1016/j.pocean.2020.102268.

788 Many, G., Bourrin, F., Durrieu de Madron, X., Ody, A., Doxaran,
789 D., Cauchy, P., 2018. Glider and satellite monitoring of the
790 variability of the suspended particle distribution and size in the
791 Rhône ROFI. Progress in Oceanography 163, 123–135. URL:
792 https://linkinghub.elsevier.com/retrieve/pii/S0079661117300502,
793 doi:10.1016/j.pocean.2017.05.006.

794 Many, G., Bourrin, F., Durrieu de Madron, X., Pairaud, I., Gan-
795 gloff, A., Doxaran, D., Ody, A., Verney, R., Menniti, C., Le Berre,
796 D., Jacquet, M., 2016. Particle assemblage characterization in the
797 Rhone River ROFI. Journal of Marine Systems 157, 39–51. URL:

https://linkinghub.elsevier.com/retrieve/pii/S0924796315002353, doi:10.1016/j.jmarsys.2015.12.010.

Marsaleix, P., Auclair, F., Duhaut, T., Estournel, C., Nguyen, C., Ulses, C., 2012. Alternatives to the Robert–Asselin filter. Ocean Modelling 41, 53–66. URL: https://linkinghub.elsevier.com/retrieve/pii/S1463500311001788, doi:10.1016/j.ocemod.2011.11.002.

Marsaleix, P., Auclair, F., Estournel, C., 2009a. Low-order pressure gradient schemes in sigma coordinate models: The seamount test revisited. Ocean Modelling 30, 169–177. URL: https://linkinghub.elsevier.com/retrieve/pii/S1463500309001358, doi:10.1016/j.ocemod.2009.06.011.

Marsaleix, P., Auclair, F., Floor, J.W., Herrmann, M.J., Estournel, C., Pairaud, I., Ulses, C., 2008. Energy conservation issues in sigma-coordinate free-surface ocean models. Ocean Modelling 20, 61–89. URL: https://linkinghub.elsevier.com/retrieve/pii/S1463500307000984, doi:10.1016/j.ocemod.2007.07.005.

Marsaleix, P., Estournel, C., Kondrachoff, V., Vehil, R., 1998. A numerical study of the formation of the Rhône River plume. Journal of Marine Systems 14, 99–115. URL: https://linkinghub.elsevier.com/retrieve/pii/S0924796397000110, doi:10.1016/S0924-7963(97)00011-0.

Marsaleix, P., Ulses, C., Pairaud, I., Herrmann, M.J., Floor, J.W., Estournel,

C., Auclair, F., 2009b. Open boundary conditions for internal gravity wave modelling using polarization relations. Ocean Modelling 29, 27–42. URL: https://linkinghub.elsevier.com/retrieve/pii/S1463500309000419, doi:10.1016/j.ocemod.2009.02.010.

Marshall, J., Hill, C., Perelman, L., Adcroft, A., 1997. Hydrostatic, quasi-hydrostatic, and nonhydrostatic ocean modeling. Journal of Geophysical Research: Oceans 102, 5733–5752. URL: http://doi.wiley.com/10.1029/96JC02776, doi:10.1029/96JC02776.

Marzocchi, A., Hirschi, J.J.M., Holliday, N.P., Cunningham, S.A., Blaker, A.T., Coward, A.C., 2015. The North Atlantic subpolar circulation in an eddy-resolving global ocean model. Journal of Marine Systems 142, 126–143. URL: https://linkinghub.elsevier.com/retrieve/pii/S0924796314002437, doi:10.1016/j.jmarsys.2014.10.007.

McCarthy, G.D., Haigh, I.D., Hirschi, J.J.M., Grist, J.P., Smeed, D.A., 2015. Ocean impact on decadal Atlantic climate variability revealed by sea-level observations. Nature 521, 508–510. URL: http://www.nature.com/articles/nature14491, doi:10.1038/nature14491.

McDougall, T.J., Greatbatch, R.J., Lu, Y., 2002. On Conservation Equations in Oceanography: How Accurate Are Boussinesq Ocean Models? Journal of Physical Oceanography 32, 1574–1584. URL: http://journals.ametsoc.org/doi/10.1175/1520-0485(2002)032<1574:OCEIOH>2.0.CO;2, doi:10.1175/1520-0485(2002)032¡1574:OCEIOH¿2.0.CO;2.

Mentaschi, L., Besio, G., Cassola, F., Mazzino, A., 2013. Problems in RMSE-based wave model validations. Ocean Modelling 72, 53–58. URL: https://linkinghub.elsevier.com/retrieve/pii/S1463500313001418, doi:10.1016/j.ocemod.2013.08.003.

Michaud, H., Marsaleix, P., Leredde, Y., Estournel, C., Bourrin, F., Lyard, F., Mayet, C., Ardhuin, F., 2012. Three-dimensional modelling of wave-induced current from the surf zone to the inner shelf. Ocean Science 8, 657–681. URL: https://os.copernicus.org/articles/8/657/2012/, doi:10.5194/os-8-657-2012.

Mikolajczak, G., 2019. Dynamique de l'eau et des apports particulaires originaires du Rhône sur la marge continentale du Golfe du Lion. Ph.D. thesis. Toulouse university, France.

Mikolajczak, G., Estournel, C., Ulses, C., Marsaleix, P., Bourrin, F., Martín, J., Pairaud, I., Puig, P., Leredde, Y., Many, G., Seyfried, L., Durrieu de Madron, X., 2020. Impact of storms on residence times and export of coastal waters during a mild autumn/winter period in the Gulf of Lion. Continental Shelf Research 207, 104192. URL: https://linkinghub.elsevier.com/retrieve/pii/S0278434320301485, doi:10.1016/j.csr.2020.104192.

Millot, C., 1990. The Gulf of Lions' hydrodynamics. Continental Shelf Research 10, 885–894. URL: https://linkinghub.elsevier.com/retrieve/pii/027843439090065T, doi:10.1016/0278-4343(90)90065-T.

Molcard, A., Pinardi, N., Iskandarani, M., Haidvogel, D., 2002. Wind driven general circulation of the Mediterranean Sea simulated with a Spectral Element Ocean Model. Dynamics of Atmospheres and Oceans 35, 97–130. URL: https://linkinghub.elsevier.com/retrieve/pii/S037702650100080X, doi:10.1016/S0377-0265(01)00080-X.

Moore, A.M., Arango, H.G., Broquet, G., Powell, B.S., Weaver, A.T., Zavala-Garay, J., 2011. The Regional Ocean Modeling System (ROMS) 4-dimensional variational data assimilation systems. Progress in Oceanography 91, 34–49. URL: https://linkinghub.elsevier.com/retrieve/pii/S0079661111000516, doi:10.1016/j.pocean.2011.05.004.

Pairaud, I., Gatti, J., Bensoussan, N., Verney, R., Garreau, P., 2011. Hydrology and circulation in a coastal area off Marseille: Validation of a nested 3D model with observations. Journal of Marine Systems 88, 20–33. URL: https://linkinghub.elsevier.com/retrieve/pii/S092479631100039X, doi:10.1016/j.jmarsys.2011.02.010.

Petrenko, A., Leredde, Y., Marsaleix, P., 2005. Circulation in a stratified and wind-forced Gulf of Lions, NW Mediterranean Sea: in situ and modeling data. Continental Shelf Research 25, 7–27. URL: https://linkinghub.elsevier.com/retrieve/pii/S0278434304002146, doi:10.1016/j.csr.2004.09.004.

Prandtl, L., 1925. Bericht über untersuchungen zur ausgebildeten turbu-

lenz. ZAMM-Journal of Applied Mathematics and Mechanics/Zeitschrift für Angewandte Mathematik und Mechanik 5, 136–139.

Putman, N., 2018. Marine migrations. Current Biology 28, R972–R976. URL: https://linkinghub.elsevier.com/retrieve/pii/S0960982218309357, doi:10.1016/j.cub.2018.07.036.

Putman, N.F., He, R., 2013. Tracking the long-distance dispersal of marine organisms: sensitivity to ocean model resolution. Journal of The Royal Society Interface 10, 20120979. URL: https://royalsocietypublishing.org/doi/10.1098/rsif.2012.0979, doi:10.1098/rsif.2012.0979.

Reffray, G., Frauni, P., Marsaleix, P., 2004. Secondary flows induced by wind forcing in the Rhne region of freshwater influence. Ocean Dynamics 54, 179–196. URL: http://link.springer.com/10.1007/s10236-003-0079-y, doi:10.1007/s10236-003-0079-y.

Renault, L., Chiggiato, J., Warner, J.C., Gomez, M., Vizoso, G., Tintoré, J., 2012. Coupled atmosphere-ocean-wave simulations of a storm event over the Gulf of Lion and Balearic Sea: COUPLED ATMOSPHERE-OCEAN-WAVE SIMULATION. Journal of Geophysical Research: Oceans 117, n/a–n/a. URL: http://doi.wiley.com/10.1029/2012JC007924, doi:10.1029/2012JC007924.

Ridenour, N.A., Hu, X., Jafarikhasragh, S., Landy, J.C., Lukovich, J.V., Stadnyk, T.A., Sydor, K., Myers, P.G., Barber, D.G., 2019. Sensitivity of

freshwater dynamics to ocean model resolution and river discharge forcing in the Hudson Bay Complex. Journal of Marine Systems 196, 48–64. URL: https://linkinghub.elsevier.com/retrieve/pii/S092479631830294X, doi:10.1016/j.jmarsys.2019.04.002.

Ringler, T., Petersen, M., Higdon, R.L., Jacobsen, D., Jones, P.W., Maltrud, M., 2013. A multi-resolution approach to global ocean modeling. Ocean Modelling 69, 211–232. URL: https://linkinghub.elsevier.com/retrieve/pii/S1463500313000760, doi:10.1016/j.ocemod.2013.04.010.

Schaeffer, A., Garreau, P., Molcard, A., Fraunié, P., Seity, Y., 2011. Influence of high-resolution wind forcing on hydrodynamic modeling of the Gulf of Lions. Ocean Dynamics 61, 1823–1844. URL: http://link.springer.com/10.1007/s10236-011-0442-3, doi:10.1007/s10236-011-0442-3.

Schroeder, K., Millot, C., Bengara, L., Ben Ismail, S., Bensi, M., Borghini, M., Budillon, G., Cardin, V., Coppola, L., Curtil, C., Drago, A., El Moumni, B., Font, J., Fuda, J.L., García-Lafuente, J., Gasparini, G.P., Kontoyiannis, H., Lefevre, D., Puig, P., Raimbault, P., Rougier, G., Salat, J., Sammari, C., Sánchez Garrido, J.C., Sanchez-Roman, A., Sparnocchia, S., Tamburini, C., Taupier-Letage, I., Theocharis, A., Vargas-Yáñez, M., Vetrano, A., 2013. Long-term monitoring programme of the hydrological variability in the Mediterranean Sea: a first overview of the HYDROCHANGES network. Ocean Science 9, 301–324. URL:

https://os.copernicus.org/articles/9/301/2013/, doi:10.5194/os-9-301-2013.

Seyfried, L., Marsaleix, P., Richard, E., Estournel, C., 2017. Modelling deep-water formation in the north-west Mediterranean Sea with a new air–sea coupled model: sensitivity to turbulent flux parameterizations. Ocean Science 13, 1093–1112. URL: https://os.copernicus.org/articles/13/1093/2017/, doi:10.5194/os-13-1093-2017.

Siedler, G., Gould, J., Church, J.A. (Eds.), 2001. Ocean circulation and climate: observing and modelling the global ocean. Elsevier Ltd.

Smith, S.D., 1988. Coefficients for sea surface wind stress, heat flux, and wind profiles as a function of wind speed and temperature. Journal of Geophysical Research 93, 15467. URL: http://doi.wiley.com/10.1029/JC093iC12p15467, doi:10.1029/JC093iC12p15467.

Somot, S., Sevault, F., Déqué, M., Crépon, M., 2008. 21st century climate change scenario for the Mediterranean using a coupled atmosphere–ocean regional climate model. Global and Planetary Change 63, 112–126. URL: https://linkinghub.elsevier.com/retrieve/pii/S0921818107001774, doi:10.1016/j.gloplacha.2007.10.003.

Thoppil, P.G., Richman, J.G., Hogan, P.J., 2011. Energetics of a global ocean circulation model compared to observations: ENERGETICS OF THE GLOBAL OCEAN. Geophysical Research

Letters 38. URL: http://doi.wiley.com/10.1029/2011GL048347, doi:10.1029/2011GL048347.

Ulses, C., Estournel, C., Puig, P., Durrieu de Madron, X., Marsaleix, P., 2008. Dense shelf water cascading in the northwestern Mediterranean during the cold winter 2005: Quantification of the export through the Gulf of Lion and the Catalan margin: CASCADING IN THE MEDITERRANEAN SEA. Geophysical Research Letters 35, n/a–n/a. URL: http://doi.wiley.com/10.1029/2008GL033257, doi:10.1029/2008GL033257.

Warner, J.C., Sherwood, C.R., Signell, R.P., Harris, C.K., Arango, H.G., 2008. Development of a three-dimensional, regional, coupled wave, current, and sediment-transport model. Computers & Geosciences 34, 1284–1306. URL: https://linkinghub.elsevier.com/retrieve/pii/S0098300408000563, doi:10.1016/j.cageo.2008.02.012.

Yang, Z., Khangaonkar, T., 2009. Modeling tidal circulation and stratification in Skagit River estuary using an unstructured grid ocean model. Ocean Modelling 28, 34–49. URL: https://linkinghub.elsevier.com/retrieve/pii/S1463500308001029, doi:10.1016/j.ocemod.2008.07.004.

Zhang, J.x., Sukhodolov, A.N., Liu, H., 2014. Non-hydrostatic versus hydrostatic modelings of free surface flows. Journal of Hydrodynamics 26, 512–522. URL:

983 http://link.springer.com/10.1016/S1001-6058(14)60058-5,
984 doi:10.1016/S1001-6058(14)60058-5.

List of Tables

List of Figures

Table 1: *Timetable of acquired flow speed data per observation station. X indicates there was data available during this month.*

Year	2010	2011	2012	2013
Month	J F M A M J J A S O N D	J F M A M J J A S O N D	J F M A M J J A S O N D	J F M A M J
Creus	X X X X X X X X X	X X X X X X X X X	X X X X X X	
LD	X X X X X X X X X X X X	X X X X X X X X X X X X	X X X X X X X X X X X X	
Lion	X X X X X X X X X X X X	X X X X X X X X X X X X	X X X X X X X X X X X X	X X X X X X
Planier	X X X X X X X X X X X X	X X X X X X X X X X X X	X X X X X X X X X X X X	
Mesurho	X X	X X X X X X	X X X X X X X X	X X X X
POEM		X X X		
SOLA	X X X			
BeSete	X X X X X X X X X X	X	X X X X X X	X X X X

Station / Indicator	Creus	LD	Lion	Planier	Mesurho	POEM	SOLA	BeSete	Mean per indicator
RMSE	50	56	58	25	59	50	33	25	45
Bias	50	41	28	42	32	0	0	42	29
HH	28	30	19	17	9	0	0	0	13
SI	33	33	25	21	27	50	33	0	28
Relative bias	28	22	17	24	21	0	0	23	17
Correlation	33	22	27	25	36	0	0	17	20
Mean per station	37	34	29	26	31	17	11	18	25
Nr of events	18	27	36	24	22	2	3	12	

Table 2: *Proportion of events worse during the event than during the reference period per indicator and per station for wind event type.*

Station / Indicator	Creus	LD	Lion	Planier	Mesurho	POEM	SOLA	BeSete	Mean per indicator
RMSE	67	40	40	20	67	100	0	100	54
Bias	67	40	40	60	33	100	0	0	43
HH	0	20	20	20	0	100	0	0	20
SI	0	20	0	40	0	0	100	0	20
Relative bias	0	20	20	20	33	100	100	0	37
Correlation	0	40	60	40	33	0	0	100	34
Mean per station	22	30	30	33	28	67	33	33	35
Nr of events	3	5	5	5	3	1	1	1	

Table 3: *Proportion of events worse during the event than during the reference period per indicator and per station for wave event type.*

Station / Indicator	POEM	BeSete	Mean per indicator
RMSE	33	25	29
Bias	33	50	42
HH	33	25	29
SI	67	25	46
Relative bias	0	0	0
Correlation	33	25	29
Mean per station	33	25	29
Nr of events	3	4	

Table 4: *Proportion of events worse during the event than during the reference period per indicator and per station for stratification event type.*

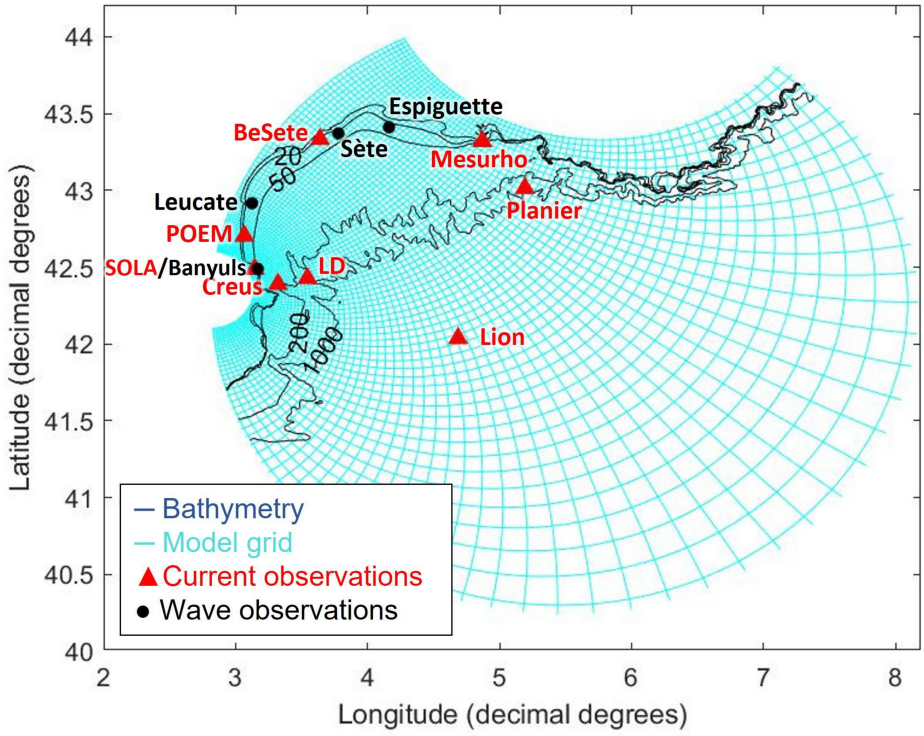

Figure 1: *The Gulf of Lion. Main bathymetrical contours (20, 50, 200, 1000 m) of the Gulf of Lion including the dipolar model grid (680 × 710; with one blue line every 10 cells; North pole (44.2°N, 5.3°E); South pole (42.37°N, 2.82°E); grid point (170; 710) corresponding to (47°N, S°E); and the reference latitude for Mercator projection was 52° N). Further information on the grid can be found in Briton et al., (2018). The locations of the fixed moorings with current meters are in red: BeSete, Creus, LD (Lacaze-Duthiers), Lion, Mesurho (Measuring buoy at the mouth of the Rhône River), Planier, POEM (Observational Platform of the Mediterranean Environment/Plateforme d'Observation de l'Environnement Méditerranéen), SOLA (SOMLIT Observatory of the Arago Laboratory/SOMLIT Observatoire de Laboratoire Arago) and with wave buoy in black: Banyuls, Espiguette, Leucate, Sète.*

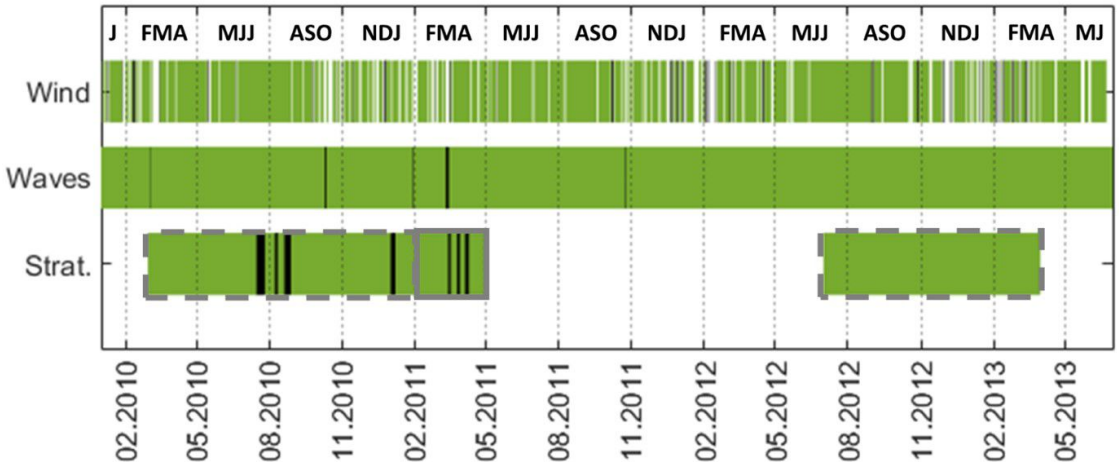

Figure 2: *Timetable with selected events (Black). Green is the reference period. For the wind events, the white zones are zones with intermediate wind. The wind and wave events are common to all stations. For the stratification event, striped line (- -) is the reference period for Besete and the full line (-) is the reference period for POEM. In the white zone, no observational data was available for these two stations. The dashed vertical lines (:) indicate the seasons and the letter triplets are the first letters of the months in that season.*

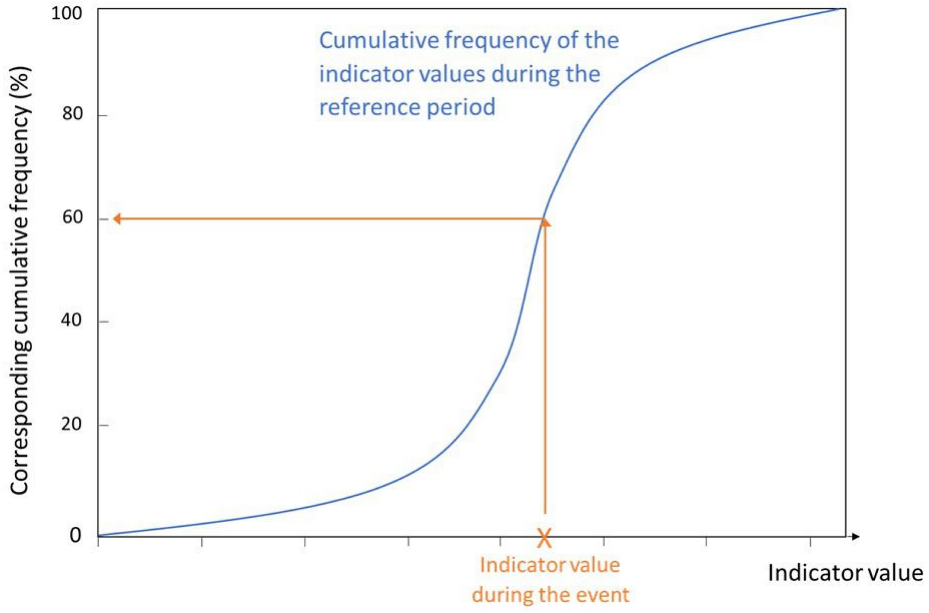

Figure 3: *Corresponding cumulative frequency example. The corresponding cumulative frequency of the indicator value during the event can be read on the y-axis of when placing the indicator value calculated during the event (orange X) on the cumulative frequency of the indicator values during the reference period (blue line).*

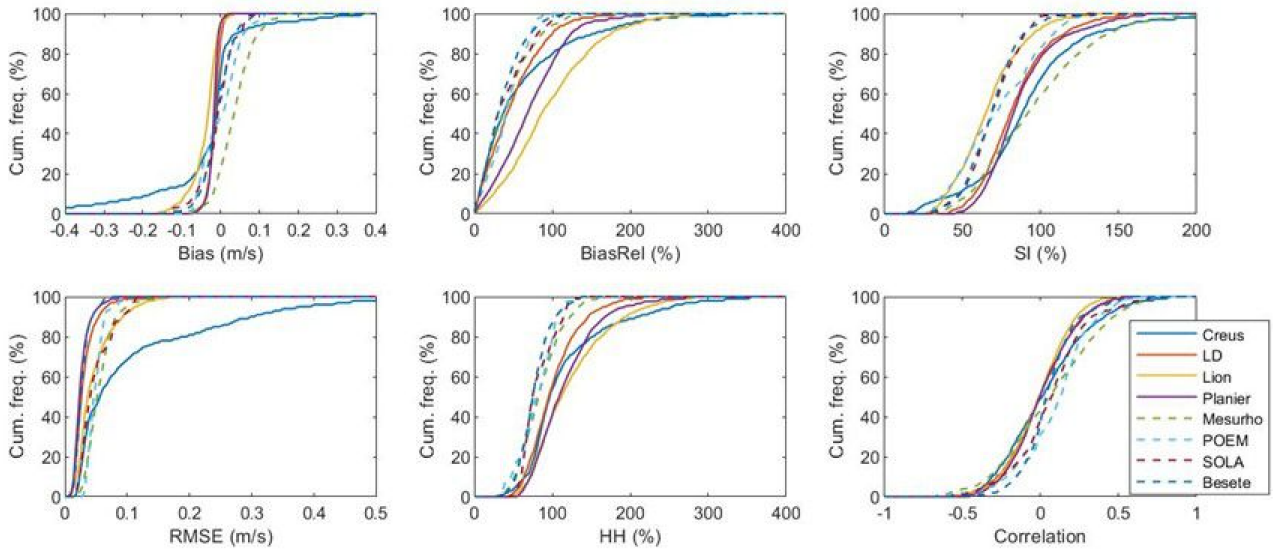

Figure 4: *42 hr reference period CFD. The indicators' cumulative frequencies integrated over 42 hr at all stations during the reference period. Shallow stations are depicted with a dashed line, deep stations with a solid line. A) Bias, B) Relative bias, C) SI, D) RMSE, E) HH, F) Correlation.*

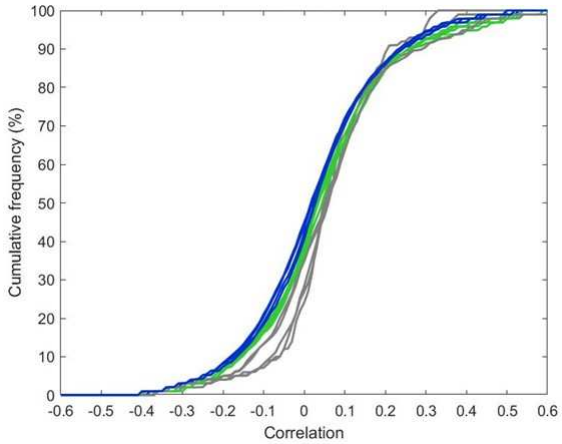

Figure 5: *CFD of the correlation between modelled and observed flow speeds at BeSete during the reference period for different durations. Blue: 12-24hr, green: 24-72hr and grey: more than 72 hr.*

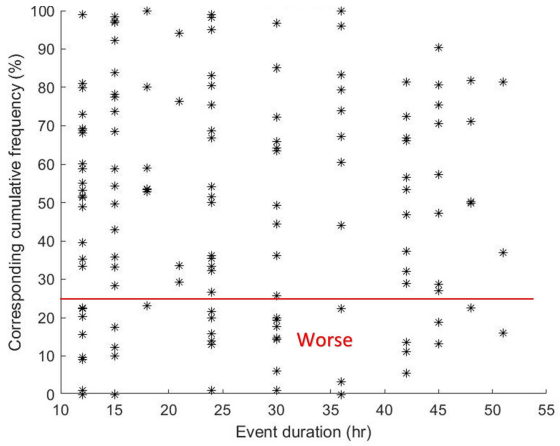

Figure 6: *Corresponding cumulative frequency of the wind's correlation. Scatter plot of the wind event duration in relation to the corresponding cumulative frequency of the correlation between modelled and observed current speed. Events with a corresponding cumulative frequency below 25% are considered worse during the event than during the reference period.*

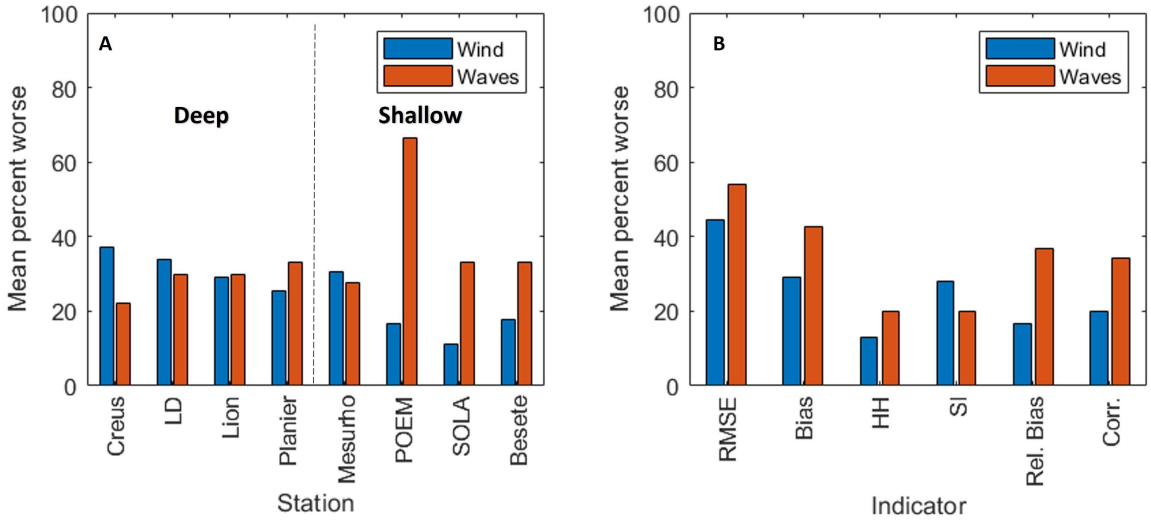

Figure 7: *Mean percent worse per station and indicator for wind and wave events. Histograms of the mean percent of wind/wave events worse during the events than during the reference period. A) Per station, B) Per indicator.*

Appendix A. Supplementary material

Table A.1: *Overview of all ocean current observation stations with the number of bins, the bin size, the depth, the time step, the type of equipment, the latitude, the longitude and the source. For the ADCPs, only the maximum depth is indicated (*).*

Station name	Creus	LD	Lion	Planier	Mesurho	POEM	SOLA	BeSete (2010-2011)	BeSete (2012-2013)
Nr of bins	1	2	5	2	40	65	26	99	54
Bin size (m)	x	x	x	x	0.75	0.5	1.0	0.25	0.5
Depth (m)	295	505 975	152 246 501 1002 2330	505 975	18.7*	28.1*	24.9*	24.6*	24.4*
Time step (min)	30	60	30	60	10	60	20	20	20
Equipment (Frequency)	SP-ADCM (2MHz)				ADCP (600 KHz)				
Latitude	42.39	42.428050	42.037267	43.015083	43.32	42.704167	42.488333	43.333917	43.333917
Longitude	3.21667	3.544783	4.686133	5.192133	4.87	3.06667	3.145	3.639617	3.639617
Source	Schroeder et al. (2013)	Durrieu de Madron et al. (2019)	Testor et al. (2019) Houpert et al. (2016)	Durrieu de Madron et al. (2019)	Pairaud et al. (2016)	Bourin et al. (2015)	Unpublished Guizien	Unpublished Leredde	

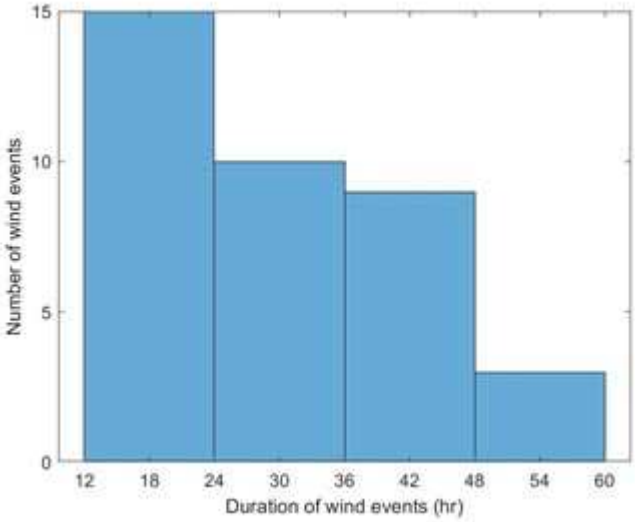

Figure A.1: *Frequency histogram of the durations of the wind events.*

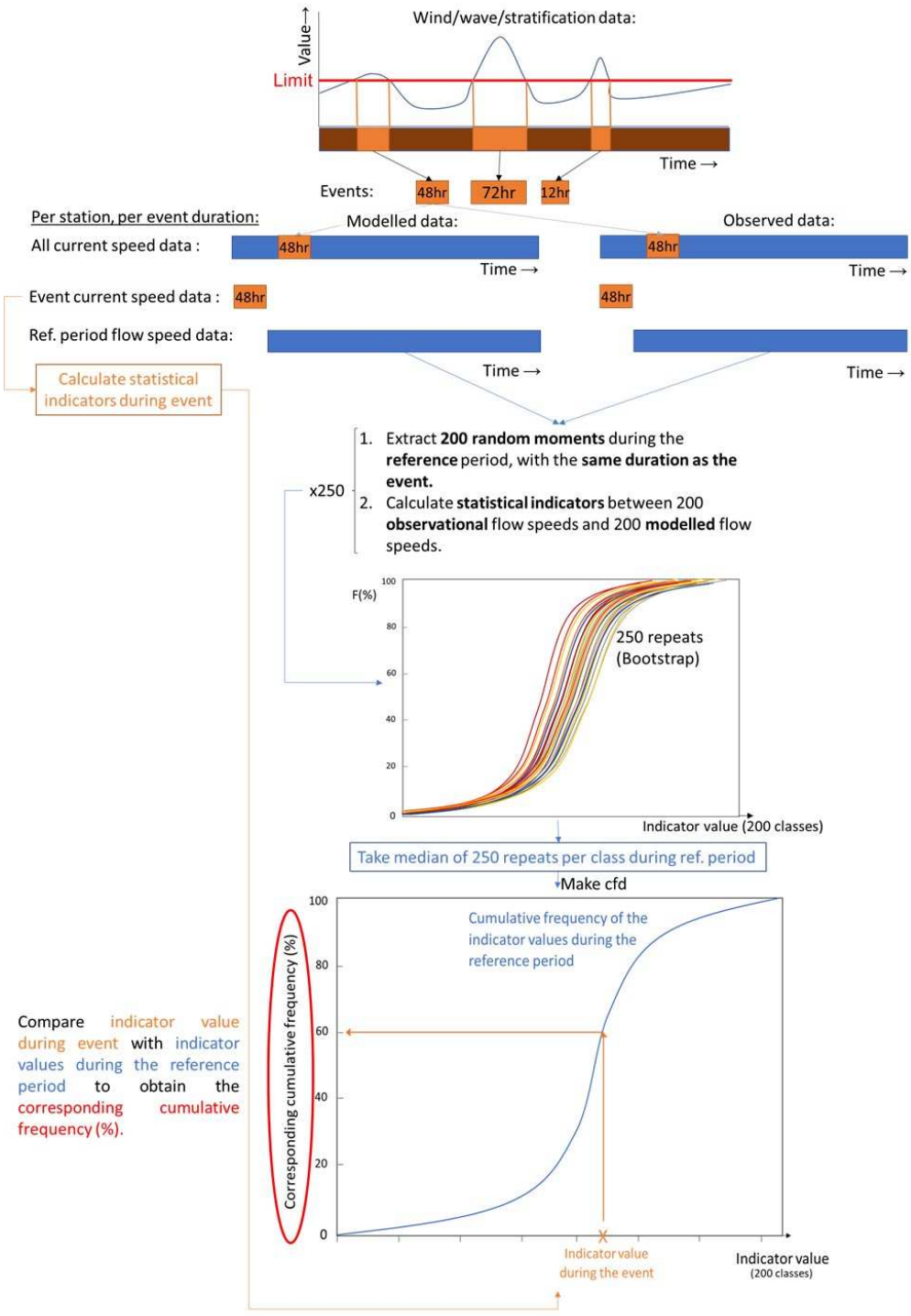

Figure A.2: *Scheme on how to compare the uncertainty of the model during the event to the uncertainty of the model outside of the events.*

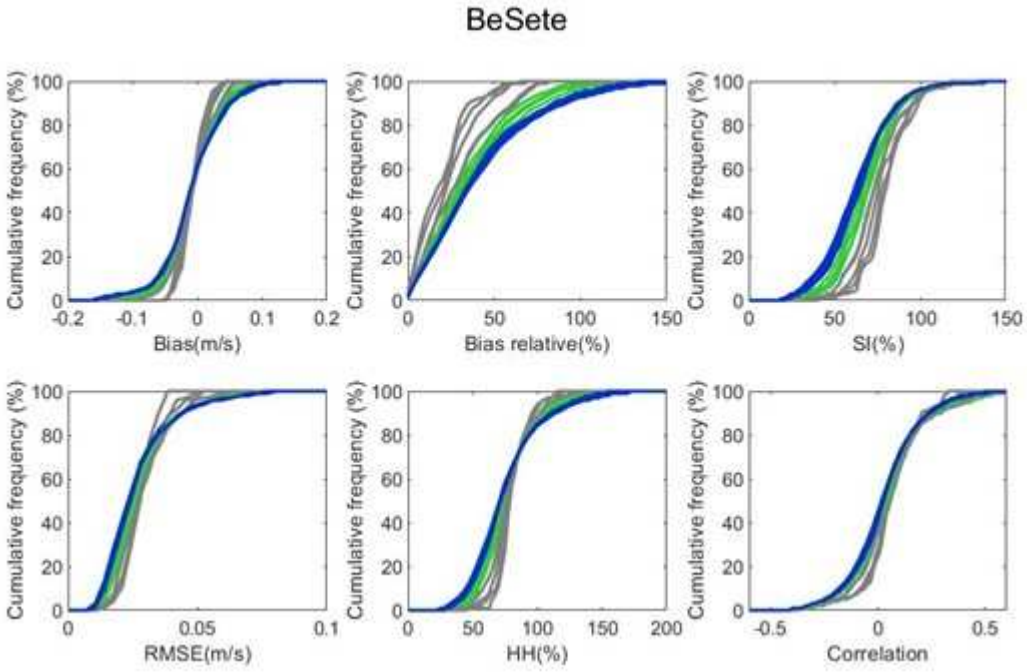

Figure A.3: *Cumulative frequency distribution of the indicators calculated between modelled and observed flow speeds at BeSete during the reference period for different durations. Blue: 12-24hr, green: 24-72hr and grey: more than 72hr.*